Single-Molecule Colocalization of Redox Reactions on Semiconductor Photocatalysts Connects Surface Heterogeneity and Charge-Carrier Separation in Bismuth Oxybromide

Meikun Shen[1], Tianben Ding[2], William H. Rackers[1], Che Tan[3], Khalid Mahmood[1], Matthew D. Lew[2,4], Bryce Sadtler[1,4]*

[1] Department of Chemistry, Washington University, St. Louis, Missouri 63130, United States

[2] Department of Electrical and Systems Engineering, Washington University, St. Louis, Missouri 63130, United States

[3] Department of Energy, Environmental & Chemical Engineering, Washington University, St. Louis, Missouri 63130, United States

[4] Institute of Materials Science & Engineering, Washington University, St. Louis, Missouri 63130, United States

Abstract

The surface structure of semiconductor photocatalysts controls the efficiency of charge-carrier extraction during photocatalytic reactions. However, understanding the connection between surface heterogeneity and the locations where photogenerated charge carriers are preferentially extracted is challenging. Herein, we use single-molecule fluorescence imaging to map the spatial distribution of active regions and quantify the activity for both photocatalytic oxidation and reduction reactions on individual bismuth oxybromide (BiOBr) nanoplates. Through a coordinate-based colocalization analysis, we quantify the spatial correlation between the locations where fluorogenic probe molecules are oxidized and reduced on the surface of individual nanoplates. Surprisingly, we observed two distinct photochemical behaviors for BiOBr particles prepared within the same batch, which exhibit either predominantly uncorrelated activity where electrons and holes are extracted from different sites or colocalized activity in which oxidation and reduction take place within the same nanoscale regions. By analyzing the emissive properties of the fluorogenic probes, we propose that electrons and holes colocalize at defect-deficient regions, while defects promote the selective extraction of one carrier type by trapping either electrons or holes. While previous work has used defect engineering to enhance the activity of bismuth oxyhalides and other semiconductor photocatalysts for useful reductive half-reactions (e.g., CO_2 or N_2 reduction), our results show that defect-free regions are needed to promote both oxidation and reduction in fuel-generating photocatalysts that do not rely on sacrificial reagents.

Introduction

Semiconductor nanocrystals are widely studied as promising photocatalysts that can use solar energy to produce fuels and commodity chemicals. Photogenerated charge carriers (i.e., electrons and holes) migrate to the surface of the particle to initiate the reduction or oxidation of species on the surface of the photocatalyst. However, the useful extraction of charge carriers competes with processes including carrier recombination and photoinduced corrosion (i.e., self-reduction or oxidation of the semiconductor) that limit the efficiency of solar-fuel production. The surface structure of semiconductor photocatalysts plays a critical role in controlling both the spatial distribution and the efficiency of charge-carrier extraction. Numerous studies have shown that systematic variations in particle shape[1-8] and defect concentration[9-20] can tune the activity of semiconductor photocatalysts. However, conventional methods of measuring the yield of chemical products only provide an ensemble average of catalytic activity that mask both inter- and intra-particle heterogeneity. Local variations in structure that arise from defects, impurities, or surface reconstruction lead to heterogeneous reaction sites across the surface of the particle. Thus, methods that avoid ensemble averaging and image the activity of individual photocatalyst particles are critical in revealing how nano- to microscale variations in surface structure affect the spatial distribution of active regions.

Photolabeling strategies have previously been employed to mark the locations where photogenerated charge carriers are extracted from individual semiconductor particles. For example, the photodeposition of metal salts has been used to identify facet-selective charge separation in microscale crystals where electrons and holes are preferentially extracted from different facets.[8, 21-32] However, this ex-situ technique (where electron microscopy is used to image the deposits after the reaction) cannot quantify variations in photocatalytic activity among different particles.

Furthermore, the initial deposition of metal or metal oxide particles on the semiconductor alters the pathways of subsequent photoexcited carriers,[31, 33] and the observed crystal facet-selectivity can vary significantly with both the preparation method of the particles and their chemical environment during photodeposition (e.g., solution pH and ionic strength).[22-25, 29-32] In comparison, single-molecule localization microscopy uses fluorogenic probes that are chemically activated on the surface of the catalyst particle to provide non-invasive and real-time monitoring of individual reaction events.[34-55] This method quantifies how nanoscale variations in charge-carrier extraction across the surface of a single particle contribute to its photocatalytic activity.

In this report, we combined single-molecule, super-resolution fluorescence microscopy with a coordinate-based colocalization analysis to quantify the spatial correlation between photocatalytic reactions initiated by electrons and holes on the surface of single bismuth oxybromide (BiOBr) nanoplates. Variations in surface structure[56] and the presence of defects, such as oxygen vacancies,[53] are known to affect the activity of BiOBr and BiOCl for synthetically useful photocatalytic half-reactions, including water oxidation,[16-17] O_2 reduction,[6, 12-14] CO_2 reduction,[18] and N_2 reduction.[19-20] While photodeposition of metal salts has previously been used to evidence facet-dependent charge-extraction in BiOBr microcrystals,[8, 32] we show that there are spatial variations for both photocatalytic reduction and oxidation reactions across the surface of the same facet. Single-molecule localization enables us to simultaneously visualize the spatial distribution of charge-carrier extraction and quantify the relative activity of different nanoscale regions. These measurements reveal significant heterogeneity in the catalytic activity of the BiOBr particles; while some regions are inactive, other nanoscale regions display average specific activities as high as 108 ± 42 $\mu m^{-2} \cdot min^{-1}$ for photocatalytic reduction and 342 ± 82 $\mu m^{-2} \cdot min^{-1}$ for photocatalytic oxidation of the probe molecules. While a common limitation of single-molecule, super-resolution

imaging of heterogeneous catalysis is that the reaction events cannot be directly correlated with a specific active site, our colocalization analysis provides a critical link between the activity of different nanoscale regions of the BiOBr photocatalyst and their relative concentration of trap sites. We show that photogenerated electrons and holes colocalize in nanoscale regions of the nanoplates that contain fewer defects. These colocalized regions possess higher activity for photocatalytic oxidation, whereas the activity for photocatalytic reduction is similar across both the colocalized and uncorrelated regions (i.e., regions where only photocatalytic reduction is significant). We demonstrate that the same semiconductor photocatalyst can be tailored to promote either photocatalytic reduction or oxidation reactions by tuning the concentration and distribution of surface defects. For solar fuel-generation, balancing the activity of both reductive and oxidative transformations without relying on sacrificial reagents will require stable control of the defect concentration during photocatalysis.

Results and Discussion

BiOBr nanoplates with edge lengths ranging from 1 to 3 μm and thicknesses of 10 to 20 nm were synthesized via a hydrothermal method (**Figure 1a**).[53, 57] The x-ray diffraction (XRD) pattern of the nanoplates matched the tetragonal pattern for BiOBr (PDF # 04-002-3609, **Figure S1**), and the absorption edge of the sample at 420 nm matched previous reports for BiOBr (**Figure S2**).[13-14, 19-20] Based on high-resolution transmission electron microscopy (HRTEM), the nanoplates expose the (001) facet as their basal plane (**Figures 1b**). While we cannot image individual point defects using HRTEM, the images show variations in crystallinity across the surface of the nanoplates indicating that defects are present (**Figure 1b** and **S3**). X-ray photoelectron spectra (XPS) of the nanoplates also support the presence of surface defects. The binding region for Bi 4f

electrons showed that while the dominant peaks belong to Bi^{3+}, there are also shoulder peaks at higher binding energy corresponding to Bi^{5+} (**Figure S4a**).[14, 58] XPS in the binding region for O 1s electrons showed a peak at 530.0 eV corresponding to oxygen within the BiOBr crystal as well as a shoulder peak at 531.5 eV (**Figure S4b**), indicating the presence of oxygen vacancies at the surface.[7, 14, 16, 18, 20] Both of these defects (i.e., Bi^{5+} and oxygen vacancies) have been previously correlated with enhanced photocatalytic activity in bismuth oxyhalide particles measured at the ensemble level.[6-7, 11-16, 18-20, 58]

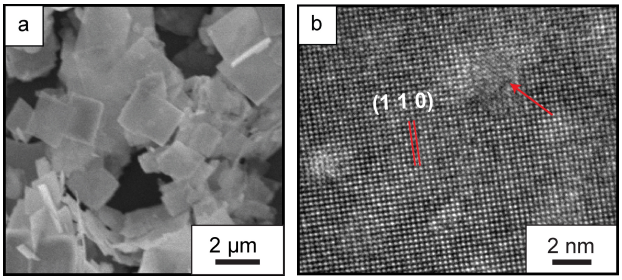

Figure 1. Structural characterization of BiOBr nanoplates. (a) Scanning electron microscopy image of BiOBr nanoplates. (b) HRTEM image of a single nanoplate. The red arrow in (b) marks a region with poorer crystallinity as seen by the less distinct lattice fringes.

We used two fluorogenic probes, resazurin and 3′-(p-aminophenyl) fluorescein (APF),[42, 45-46, 48-49, 51-53] to image charge-carrier extraction from individual BiOBr nanoplates. Photogenerated electrons in the conduction band of BiOBr can reduce resazurin to form the highly fluorescent product resorufin (**Figure 2a**), while photogenerated holes in the valence band can oxidize APF to generate fluorescein (**Figure 2d**). Hydroxylamine, NH_2OH, and potassium iodate, KIO_3, were used as sacrificial reagents to maintain charge balance during photocatalytic reduction and oxidation, respectively. We first irradiated suspensions of the BiOBr nanoplates in aqueous

solutions containing either resazurin (40 nM) and NH_2OH (1 μM) or APF (30 nM) and KIO_3 (1 μM) with a 405-nm LED (i.e., above the bandgap of BiOBr, see **Figure S2**). Fluorescence spectra show that the emission intensity of resorufin (using resazurin) or fluorescein (using APF) increases with irradiation time, indicating that BiOBr can photochemically activate both probe molecules at the ensemble level (**Figure S5**).

We then used total internal reflection fluorescence (TIRF) microscopy to image the activation of individual probe molecules on the surface of BiOBr nanoplates. The nanoplates were spin coated onto glass coverslips, and 100 μL of the probe solution was added to the coverslip (i.e., either 40 nM of resazurin and 1 μM of NH_2OH or 40 nM of APF and 1 μM of KIO_3). While the SEM image in **Figure 1a** (prepared by drop casting) shows aggregates of particles, spin coating dilute solutions of the particles led to primarily individual nanoplates dispersed on the coverslip. Stacked nanoplates could be identified by differential interference contrast (DIC) microscopy (**Figure S6**), and these particles were avoided for single-molecule imaging. We next used a 405-nm laser to excite the BiOBr nanoplates. A 561-nm laser was used to excite resorufin molecules when imaging the reduction of resazurin, and a 488-nm laser was used to excite fluorescein when imaging the oxidation of APF. The activation of either probe molecule on the surface of a nanoplate leads to a sudden turn-on in fluorescence, which we attribute to the activation of the probe. Control experiments show that because of the small amount of activated product molecules generated during imaging, re-adsorption of the product molecules is not significant (see Section 8 of the **Supporting Information** for further details). Analysis of the on-times of fluorescence bursts on BiOBr nanoplates indicates that the turn-off in single-molecule emission is due to the desorption of the activated probe from the nanoplate.[53] For each probe molecule, we then determined the centroid positions of all fluorescence bursts detected over 2500 frames (at a 50-ms

exposure time). The localization precision of fluorescence bursts using APF is 26 nm (**Figure S7**), and the precision is 21 nm using resazurin (**Figure S8**).

We next reconstructed activity maps for either photocatalytic reduction or oxidation by binning single-molecule bursts within 120 nm × 120 nm regions across the surface of individual nanoplates, as shown in **Figure 2c, f**. The color scales in the activity maps indicate the number of fluorescence bursts detected in each nanoscale region. The activity maps for both reactions show variations in the number of reaction events detected across the nanoplate surface, and this heterogeneity was observed in all particles we examined. Activity maps generated using longer imaging times with APF to probe oxidation did not show significant changes in the spatial variations in activity nor the per-nanoplate activity (see **Figure S9**). As described in our previous work,[53] when using resazurin to probe reduction events (with NH_2OH as a sacrificial reductant), the activity of the nanoplates changes due to the photochemical creation of oxygen vacancies when irradiated for longer periods of time (> 10 minutes), which is why we kept the imaging times short in these experiments (~ 2 minutes). While there are variations in activity across the surface of the nanoplates, these variations are not facet-dependent. The specific activity (i.e., the number of fluorescence bursts per unit time and per lateral area) averaged over 20 nanoplates is similar around the edges and the middle of the nanoplates for both oxidation and reduction (**Figure S10**). The on-times for fluorescence bursts are also similar indicating that the probe molecules do not preferentially adsorb around the edges nor the middle of the nanoplates. These results agree with a prior report that in aqueous solutions near neutral pH (desirable for applications in solar water splitting), both photocatalytic reduction and oxidation reactions take place on the basal (001) surfaces of BiOBr microcrystals.[32] Moreover, the *in situ* imaging method used here quantifies the

catalytic activity at different regions across the particle surface, and provides the ability to correlate spatially the extraction of photogenerated electrons and holes on the same nanoplate.

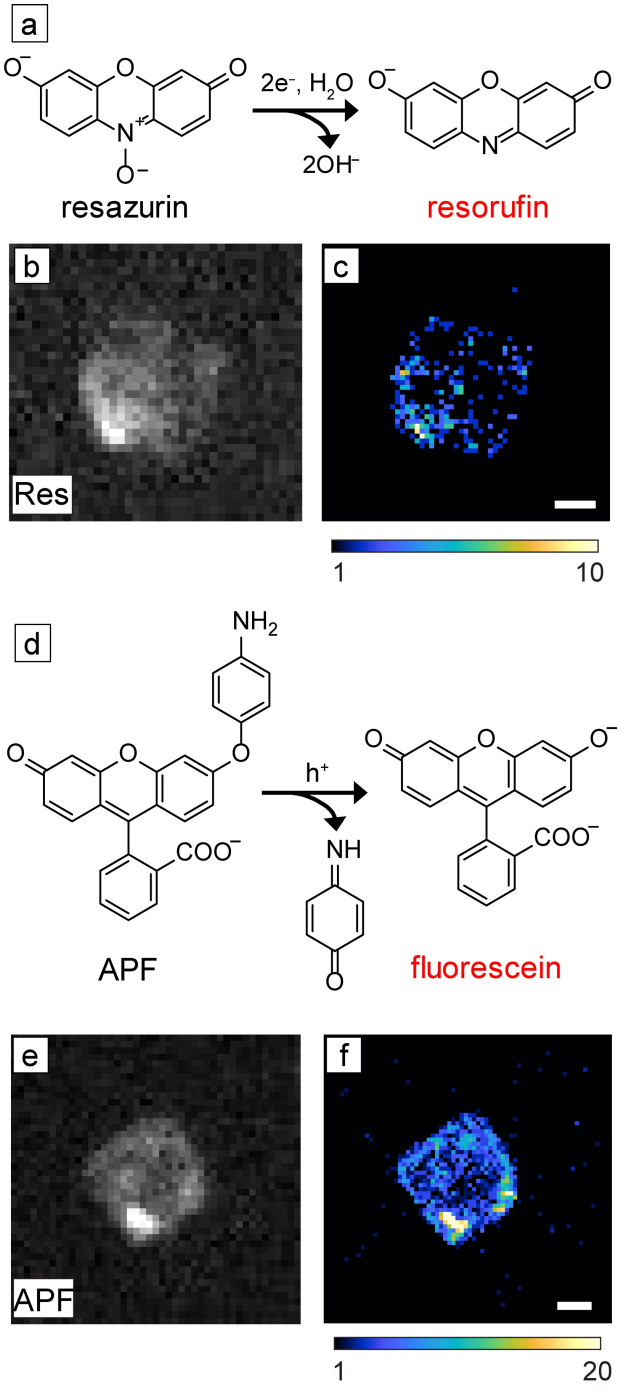

Figure 2. Single-molecule imaging of photocatalytic reduction and oxidation reactions on BiOBr nanoplates using fluorogenic probes. (a) Reductive deoxygenation of resazurin by photogenerated electrons in BiOBr produces highly fluorescent resorufin. (b) Diffraction-limited fluorescence image of a BiOBr nanoplate using resazurin as the fluorogenic probe under dual 405-nm and 561-nm laser excitation recorded at an exposure time of 50 ms. (c) Super-resolution activity map of the nanoplate in (b) for photocatalytic reduction produced by localizing the positions of all fluorescence bursts. (d) Oxidative cleavage of the aminophenyl group of 3'-(p-aminophenyl) fluorescein (APF) by photogenerated holes in BiOBr produces fluorescein. (e) Diffraction-limited fluorescence image of a different BiOBr nanoplate using APF as the fluorogenic probe under dual 405-nm and 488-nm laser excitation recorded at an exposure time of 50 ms. (f) Super-resolution activity map of the nanoplate in (e) for photocatalytic oxidation produced by localizing the positions of all fluorescence bursts. Color scales: number of fluorescence bursts per bin (120 nm × 120 nm). The white scale bars in (c) and (f) are 1 μm.

To understand the chemical origins of the spatial heterogeneity observed for both photocatalytic reduction and oxidation, we sequentially performed single-molecule imaging with APF and resazurin on the same BiOBr nanoplates (**Figure 3**). Each coverslip was washed repeatedly after imaging with the APF probe solution to remove any fluorescent residue. After washing, the number of fluorescence bursts observed was insignificant until the resazurin probe solution was added to the coverslip (**Figure S11**). Using the activity maps generated from each fluorogenic probe, we quantified the spatial correlation between oxidation and reduction reaction events with a coordinate-based colocalization (CBC) algorithm (see Section 11 of the **Supporting Information** and **Figure S12** for details on how drift correction was performed when switching

between probe solutions).[52, 59] **Figure 3** shows examples of this analysis performed on two different BiOBr nanoplates. Each fluorescence burst (i.e., reaction event) is assigned a CBC score based on its spatial proximity to the other probe's fluorescence bursts. A CBC score of +1 indicates a high spatial correlation where both oxidation and reduction events are detected in the same region, while a score of -1 indicates that only one of the two probes was detected in the region (see the **Supporting Information** for additional details on the colocalization analysis). This procedure generates a colocalization map for each probe. Orange regions in **Figure 3c, d** are nanoscale regions where oxidation and reduction are spatially colocalized. Blue regions in the left columns of **Figure 3c, d** indicate regions were only the oxidation of APF takes place. Blue regions in the right columns of **Figure 3c, d** indicate regions were only the reduction of resazurin takes place. The observed trends in the CBC scores hold when analyzing different portions of the videos collected during single-molecule imaging (see **Figure S13**). Oxidation and reduction events for the BiOBr nanoplate characterized in panels a, c, and e of **Figure 3** show a broad distribution of CBC scores (with median CBC scores of -0.14 for APF and 0.01 for resazurin) indicating a low degree of spatial correlation between the oxidation and reduction events. Interestingly, the nanoplate characterized in panels b, d, and f of **Figure 3** exhibits several nanoscale regions with a high degree of correlation between the two probes (with median CBC scores of 0.62 for APF and 0.63 for resazurin).

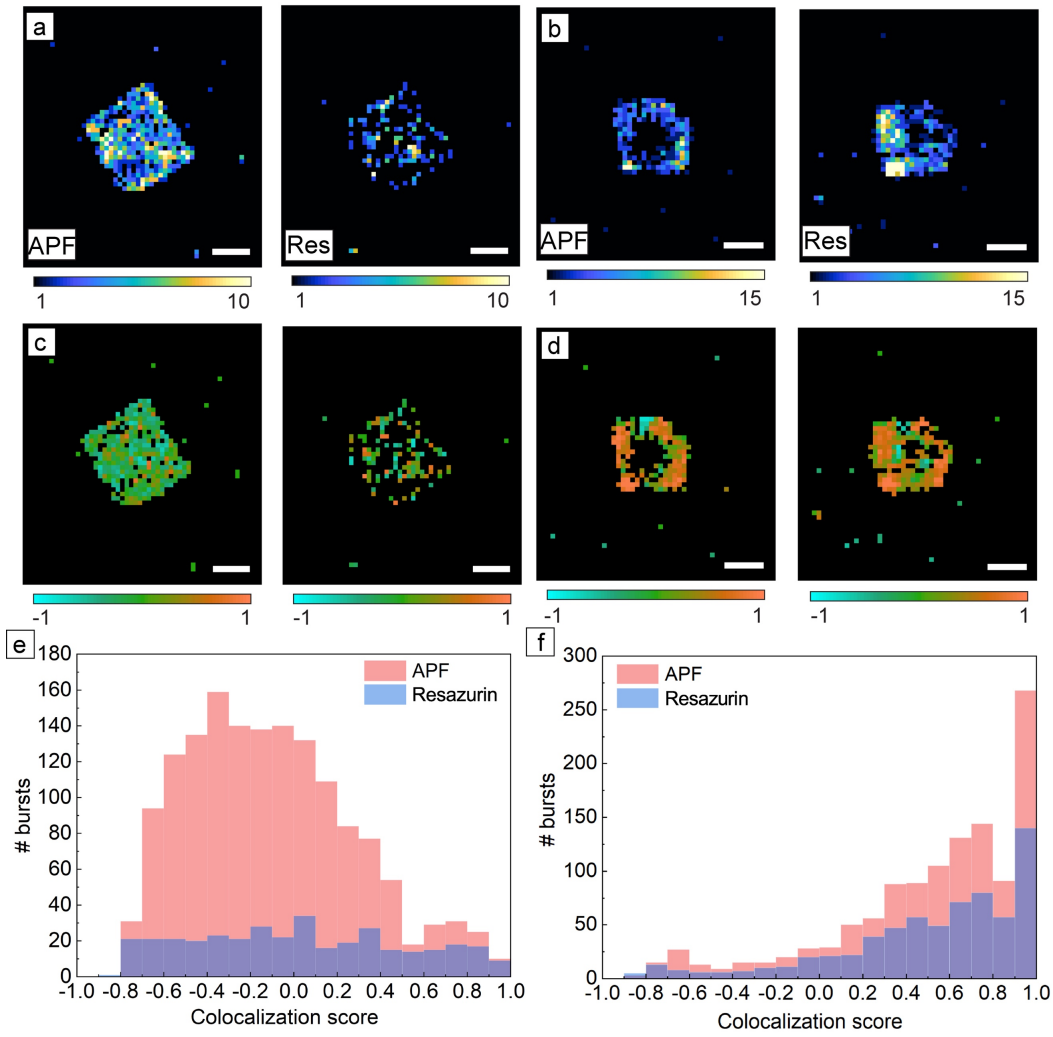

Figure 3. Colocalization of photocatalytic oxidation and reduction reactions on representative type I (a, c, and e) and type II (b, d, and f) BiOBr nanoplates. (a, b) Super-resolution activity maps of two BiOBr nanoplates using APF (1st and 3rd columns) and resazurin (2nd and 4th columns) as probes for photocatalytic oxidation and reduction, respectively. Color scale: number of fluorescence bursts per bin (120 nm × 120 nm). (c, d) Coordinate-based colocalization (CBC) maps for fluorescence bursts using APF (1st and 3rd columns) and resazurin (2nd and 4th columns). Color scale: median CBC score in each bin ranging from -1 for anti-correlated to +1 for perfectly correlated burst distributions. All white scale bars are 1 μm. (e, f) Distribution of CBC scores for

APF (red) and resazurin (blue) bursts showing low spatial correlation for the type I nanoplate in (e) and high spatial correlation for the type II nanoplate in (f).

By analyzing spatial correlations between the probes for photocatalytic oxidation and reduction, we observed two distinct behaviors among the population of BiOBr nanoplates. **Figure S14** shows the distributions of CBC scores for all fluorescence bursts detected on 46 BiOBr nanoplates using each probe. The majority of particles (30 out of 46, referred to as type I) exhibit a broad distribution of CBC scores that are peaked near a value of 0, indicating there is little spatial correlation between the two probes (see **Figures S15** and **S16** for additional examples). Specifically, the mean per nanoplate CBC scores are -0.07 ± 0.09 (mean ± 1st standard deviation) for APF and -0.04 ± 0.12 for resazurin in these type I particles. However, a portion of the nanoplates analyzed (16 particles out of 46 particles, referred to as type II) possess activity maps in which a high number of events have a CBC score above 0.9. These type II nanoplates have significantly higher CBC scores with a mean of 0.46 ± 0.18 for APF and 0.54 ± 0.14 for resazurin (see **Figures S17** and **S18** for additional examples). **Figure S19** compares the CBC scores for all fluorescence bursts detected in the two types of nanoplates. By plotting the mean CBC score of a nanoplate for reduction events vs. its score for oxidation, these two behaviors separate into distinct clusters (**Figure 4**). Type I nanoplates are grouped in the middle of the plot, while type II nanoplates (with higher spatial correlation) are grouped in the upper right.

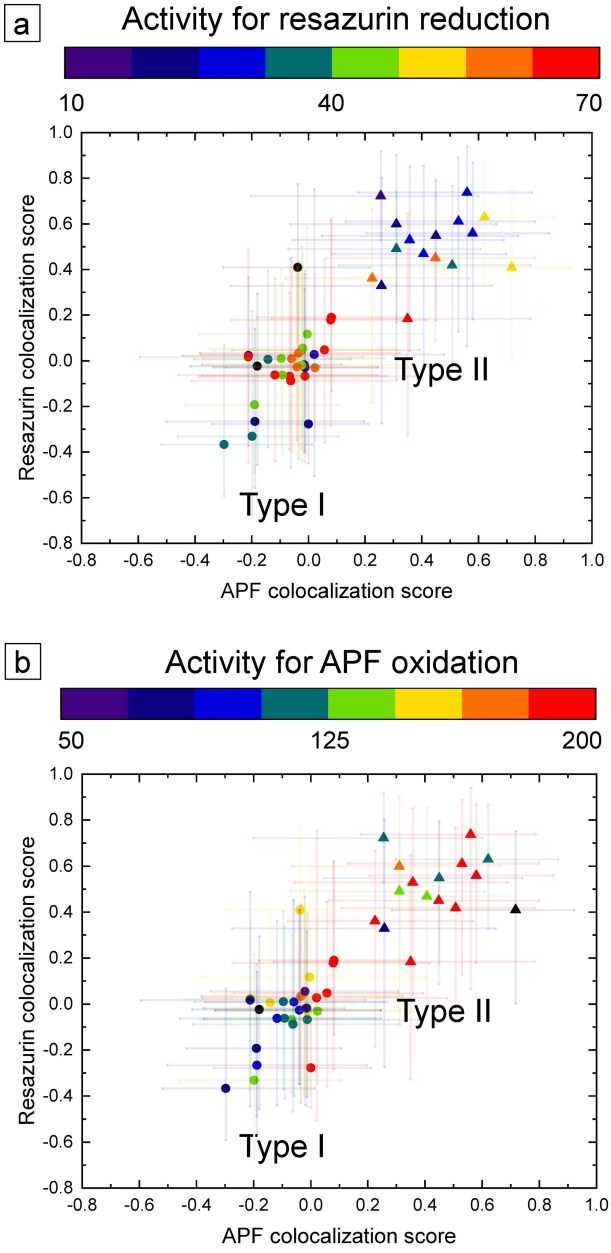

Figure 4. Per-particle CBC scores for resazurin versus APF for 46 BiOBr nanoplates. As each nanoplate exhibits a range of CBC scores for the fluorescence bursts detected on its surface, the median CBC score is denoted by a marker (circles for type I nanoplates and triangles for type II nanoplates). The lines show the 25th to 75th percentile range of CBC scores for each nanoplate. Type I (circles) and type II (triangles) nanoplates were classified using the k-means clustering algorithm with $k = 2$ (Section 11 and **Figure S19**, **Supporting Information**). The color scale in

(a) indicates the specific activity ($\mu m^{-2} \cdot min^{-1}$) of each nanoplate for the reduction of resazurin, while the color scale in (b) indicates the specific activity of each nanoplate for the oxidation of APF.

Single-molecule counting of reaction events enables us to quantify the specific activity (i.e., the number of fluorescence bursts per unit time and per lateral area) for each nanoplate. The color scales in **Figure 4** show that type I and type II particles possess different photocatalytic activities (symbols with warmer color indicate higher activity). Type I nanoplates exhibit a higher average (per nanoplate) specific activity for the photocatalytic reduction of resazurin ($52 \pm 19\ \mu m^{-2} \cdot min^{-1}$, average first ± standard deviation for 29 nanoplates) compared to the specific activity of type II nanoplates ($34 \pm 14\ \mu m^{-2} \cdot min^{-1}$ for 17 nanoplates). On the other hand, type II nanoplates exhibit higher average specific activity for the photocatalytic oxidation of APF ($192 \pm 66\ \mu m^{-2} \cdot min^{-1}$) compared to the activity of type I nanoplates ($127 \pm 51\ \mu m^{-2} \cdot min^{-1}$). Thus, the two types of nanoplates not only differ in the spatial correlation between oxidation and reduction events, but also in their activity for each reaction.

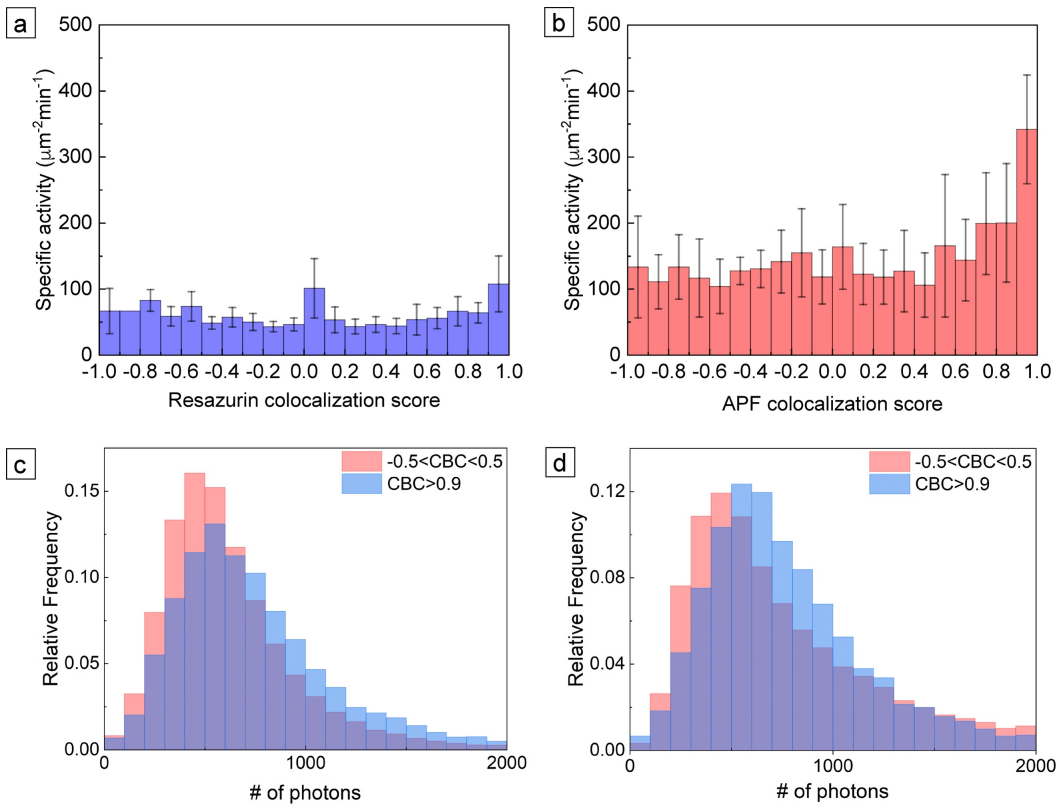

Figure 5. Specific activities and photon counts for photocatalytic reduction and oxidation as a function of the spatial correlation between probes. (a) Average specific activities of different nanoscale regions for the reduction of resazurin binned by their CBC score. (b) Average specific activities of different nanoscale regions for the oxidation of APF binned by their CBC score. The specific activity and median CBC score were calculated for each 120 nm × 120 nm region, and then a mean specific activity was calculated for all regions within a given range of CBC values (e.g., 0.9 to 1.0). Error bars show the standard deviations in activity over all regions within the given range of CBC scores. (c, d) Number of photons detected per fluorescence burst using (c) the oxidation of APF to fluorescein and (d) the reduction of resazurin to resorufin. The histograms in (c) and (d) compare fluorescence bursts with CBC scores in the range of -0.5 to 0.5 (red) to bursts with CBC scores > 0.9 (blue).

To understand how spatial colocalization of redox reactions affects the photocatalytic activity of different nanoscale regions, we extended our analysis to the sub-particle level and focus only on the catalytically active regions of the surface. We analyzed all accumulation bins (120 nm × 120 nm) in which fluorescence bursts were detected and calculated the specific activity of each region (i.e., the number of bursts detected divided by the bin area and imaging time). We then calculated the CBC score of each region (i.e., the median CBC score of all bursts detected in the bin) to compare the degree of spatial correlation to specific activity. **Figure 5** shows the average specific activities of different nanoscale regions for both probe reactions binned by their CBC score. The specific activity for the reduction of resazurin (**Figure 5a**) does not show a significant dependence on CBC score. The average specific activity of 108 ± 42 $\mu m^{-2} \cdot min^{-1}$ for photocatalytic reduction in regions with colocalized activity (i.e., 14% of all bins with median CBC scores > 0.9) is similar to the value of 94 ± 15 $\mu m^{-2} \cdot min^{-1}$ for uncorrelated regions (i.e., 69% of all bins with median CBC scores in the range of -0.5 to 0.5). Thus, the difference in activity for the reduction of resazurin does not appear to arise from an intrinsic difference in the activity of different surface sites between the two types of nanoplates. We note that some nanoplates, such as the one in **Figure 3b**, contain inactive regions (see **Figures S15** to **S20** for activity maps of additional nanoplates). The percent active area of each nanoplate was calculated by dividing the total area of bins in which at least one fluorescence burst was detected by the area of the nanoplate. For type I nanoplates, 68 ± 14% of the surface is active on average for photocatalytic reduction, while it is only 45 ± 16% for type II nanoplates. Therefore, the higher activity observed in type I nanoplates for the photocatalytic reduction of resazurin is due to a higher percentage of their surface being active for this reaction.

For photocatalytic oxidation (**Figure 5b**), regions with colocalized activity (i.e., 12% of all bins with median CBC scores > 0.9) possess a significantly higher average activity of 342 ± 82 $\mu m^{-2} \cdot min^{-1}$ compared to a value of 131 ± 46 $\mu m^{-2} \cdot min^{-1}$ for uncorrelated regions (i.e., 78% of all bins with median CBC scores in the range of -0.5 to 0.5). Both types of nanoplates possess similar active areas for the oxidation of APF with 85 ± 9% of the surface being active on average for type I nanoplates and 78 ± 15% active for type II nanoplates. Since the percentage of active area for oxidation is similar for type I and type II nanoplates, the higher per nanoplate activity observed for type II nanoplates indicates that colocalized regions contain sites that are intrinsically more active for photocatalytic oxidation.

The spatially variant activity maps combined with the higher activity of colocalized regions for photocatalytic oxidation indicate there are distinct reaction sites on the surface of each nanoplate with different chemical properties. To further understand the differences in the nature of the active regions, we compared the average photon counts and on-time of fluorescence bursts for different ranges of CBC scores. The average on-time was determined from an exponential fit of the on-times for individual fluorescence bursts. The median photon counts for bursts with CBC scores greater than 0.9 (752 ± 378 photons for resorufin and 670 ± 368 photons for fluorescein) are higher than those for uncorrelated bursts with CBC scores in the range of -0.5 to 0.5 (644 ± 409 photons for resorufin and 554 ± 319 photons for fluorescein) (**Figure 5c, d**). We confirmed that the differences in the distributions of photon counts for bursts detected at colocalized and uncorrelated regions of the catalyst surface were significant by performing a Kolmogorov–Smirnov test (K-S test, see section 12 of the **Supporting Information** and **Table S1** for details). The differences in photon counts could arise from differences in the quantum yield of the fluorogenic probe when attached to different surface sites[60] or due to differences in the

reabsorption of photons emitted from the probe by the nanoplate. However, the average on-times of fluorescence bursts with CBC scores > 0.9 (23.0 ± 0.1 ms for resorufin and 18.0 ± 0.1 ms for fluorescein) are identical to the on-times of bursts with CBC scores in the range of -0.5 to 0.5 (23.0 ± 0.1 ms for resorufin and 18.0 ± 0.1 ms for fluorescein) (**Figure S21**). The on-time of a fluorescence burst reflects the amount of time the activated probe spends on the surface of the nanoplate before desorption.[37-38, 45-46, 53] The similarities in on-times for regions with different CBC scores indicate that the binding of each product molecule (e.g., resorufin or fluorescein) is similar at different sites across the surface of the BiOBr nanoplates.

Therefore, we propose that the nanoscale regions of the BiOBr nanoplates with spatially colocalized activity reabsorb fewer photons from the activated fluorogenic probes, which makes intensity bursts from these regions brighter. Pristine BiOBr with an absorption onset of 420 nm does not absorb visible light emitted from the activated probes (i.e., emission maxima at 583 nm for resorufin and 521 nm for fluorescein). However, defects including oxygen vacancies and Bi in a reduced oxidation state increase the absorption of visible light in BiOBr by creating mid-gap defect states.[6, 11-20, 53, 58] Thus, defect-rich regions will reabsorb more photons emitted from a fluorescent probe bound to the top surface of a nanoplate and are more effective at reabsorption compared to variations in the thickness of the nanoplate (see section 13 of the **Supporting Information** for details).[61] To further test this hypothesis, defect-rich nanoplates were prepared through post-synthetic, *in-situ* photodoping at longer irradiation times than used here for fluorescence imaging (see the **Experimental Section** for details). After photodoping, the nanoplates possess a higher concentration of both oxygen vacancies and Bi^0 (while the initial BiOBr sample contains primarily Bi^{3+} with a minor amount of Bi^{5+} as shown by XPS in **Figure S4**, the photodoping process reduces a portion of both Bi^{5+} and Bi^{3+} ions at the surface of the

nanoplates).[53] The nanoplates show reduced photon counts for both probes after photodoping (**Figure S22**). The median photon counts of fluorescence bursts detected on 10 of the as-synthesized nanoplates (699 ± 325 photons for resorufin and 675 ± 429 photons for fluorescein) are significantly higher (via K-S test, **Table S1**) than for bursts detected on the same nanoplates after photodoping (561 ± 304 photons for resorufin and 427 ± 353 photons for fluorescein). These results reveal that the nanoscale regions of the nanoplates with colocalized activity (i.e., high CBC scores) possess fewer defects than regions with exclusive activity for one carrier type.

The useful extraction of photogenerated electrons or holes to induce photocatalytic reactions competes with carrier recombination, trapping, and photo-induced corrosion. The presence of a high concentration of scavenger for the charge carrier not being probed (i.e., NH_2OH to scavenge holes when imaging photocatalytic reduction and KIO_3 to scavenge electrons when imaging photocatalytic oxidation) enables us to probe each charge carrier selectively without kinetic limitations from reactions induced by the opposite charge.[62] Trapping of charge carriers at defect sites can either enhance or lower photocatalytic activity depending on the number and distribution of trap sites. Isolated defects that act as shallow trap states (i.e., that are close in energy to one of the band edges) can increase the carrier's lifetime and still allow the trapped carrier to participate in photocatalysis.[11, 13-14, 17-20, 58] For example, oxygen vacancies in BiOBr have been shown to increase the lifetime of photoexcited electrons and enhance the activity of BiOBr for the reduction of O_2, CO_2, and N_2.[14, 18-19] However, as the density of mid-gap defect states increases (at higher defect concentrations), new relaxation pathways become available that facilitate carrier recombination and lower activity.[53, 63]

Regions of the photocatalyst that are relatively free of defects should exhibit different activity than regions where either the selective trapping of electrons or holes takes place. Consistent with

this expectation, type II nanoplates with colocalized activity are more active for the oxidation of APF compared to type I nanoplates with uncorrelated activity. We postulate that regions of a nanoplate with exclusive activity for photocatalytic oxidation contain trap sites that decrease activity by mediating faster relaxation of photogenerated holes. While we cannot determine the chemical nature of these trap sites using single-molecule fluorescence, local surface reconstruction leading to an O–Bi terminated surface has been proposed to serve as a trap site for photogenerated holes in bismuth oxyhalides.[56] On the other hand, the activity for the reduction of resazurin is similar at both colocalized and uncorrelated regions. This similarity arises because the reduction of resazurin is limited by another competing process; photogenerated electrons can reduce bismuth ions on the surface of BiOBr rather than surface-adsorbed resazurin.[13, 53, 58] Thus, type I nanoplates have a higher concentration of trap sites for electrons (e.g., oxygen vacancies or Bi^{5+}) leading to predominantly uncorrelated activity between electrons and holes and more widespread reduction of resazurin across the particle surface.

Conclusion

In summary, through single-molecule localization of individual reaction events, we quantified the spatial correlation between the extraction of photogenerated electrons and holes from individual BiOBr nanoplates. We revealed two populations of particles in the same batch with either colocalized or uncorrelated activity. By comparing the degree of colocalization between reaction events using two fluorogenic probes with their emissive properties and the activity of different nanoscale regions, we elucidate that electrons and holes colocalize at defect-deficient regions of the nanoplates but separate and become trapped at defect-rich regions. While previous reports have shown that oxygen vacancies in BiOBr increase its activity for photocatalytic half-

reactions including the reduction of CO_2, and N_2 at the ensemble level, our studies reveal that defects increase the area of a nanoplate that is active for reduction and simultaneously lower its activity for oxidation. Many lab-scale studies of photocatalysis (including this one) rely on a sacrificial reagent to rapidly replenish the carrier not being studied. However, in the large-scale production of fuels via solar-driven photocatalysis, it will be more cost-effective to use the same photocatalytic particles to drive both the reductive and oxidative halves of the fuel-forming reaction (e.g., both the reduction of protons and water oxidation to produce H_2 and O_2).[64] Thus, to achieve optimal performance for a specific catalytic transformation, it will be necessary to tune the concentration and type of defects within photocatalysts such as BiOBr. When only the oxidative half-reaction is important, defect-free BiOBr particles are preferable to minimize hole trapping, whereas a higher concentration of oxygen vacancies may be desirable to increase the active area for the reductive half reaction. Ultimately, photocatalysts containing a stable intermediate concentration of defects may prove to be optimal for balancing the activity of both reductive and oxidative transformations. In the future, we plan to study how tuning the defect concentration of BiOBr particles (such as through the photodoping process described above) changes the relative populations of type I and type II nanoplates. Our colocalization analysis may be applied to other semiconductor photocatalysts that exhibit a non-uniform spatial distribution of oxidation and reduction reactions,[42, 51] as well as semiconductor heterostructures used to increase the spatial separation of photogenerated electrons and holes.[44, 65-66]

Experimental Section

Synthesis of BiOBr nanoplates. BiOBr nanoplates were synthesized using a previously reported hydrothermal method.[53, 57] The amounts of reagents were reduced by 50% compared to the original

report. First, 2.5 mmol (0.911 g) of hexadecyltrimethylammonium bromide (CTAB) was added to 50 mL of deionized water and stirred for 30 minutes. 2.5 mmol (1.213 g) of bismuth nitrate hydrate ($Bi(NO_3)_3 \bullet xH_2O$) was then added to the mixture and stirred for 20 minutes, leading to the formation of a white slurry. A freshly prepared aqueous solution of 1 M sodium hydroxide (NaOH) was added dropwise under stirring to adjust the pH of the slurry to 7. The reaction mixture was divided into two halves. Each half was transferred to a 45-mL, Teflon-lined, acid-digestion vessel (Parr Instrument Co., model 4744) and heated in an oven at 170°C for 17 hours. The reaction vessels were then removed from the oven and left in ambient air to cool to room temperature. The contents of the two reaction vessels were then transferred to two centrifuge tubes and centrifuged at 8,000 rpm for 4 minutes. The supernatant from each centrifuge tube was removed to obtain a faint yellow precipitate. The precipitates from the two centrifuge tubes were combined and washed with deionized water once and ethanol two more times. All supernatant was removed after the third wash, and the remaining precipitate was dried at 40°C in a vacuum oven at 10^{-2} atm overnight before further characterization.

Ensemble activation of fluorogenic probe molecules. Fluorescence spectroscopy was used to monitor the activation of both resazurin and APF by BiOBr nanoplates at the ensemble scale, as shown in **Figure S5**. The BiOBr powder (5 mg) was dispersed in 10 mL of an aqueous phosphate buffer solution (pH 7.4) containing either 5 μM resazurin and 1 μM NH_2OH or 5 μM APF and 1 μM KIO_3 in a glass vial. The colloidal suspension was sonicated for 1 minute and purged with argon for 30 minutes in the dark to remove dissolved oxygen before irradiation. The suspension was then irradiated under constant stirring using a high-power, light-emitting diode (Thorlabs, M405LP1). The LED has a central wavelength of 405 nm (FWHM ~ 15 nm), and an aspheric

condenser lens (Thorlabs, ACL3026) was used to collimate the light. The irradiance at the front face of the vial was 8.3 mW/cm^2. Aliquots of approximately 1 mL were collected periodically over time using a needle and syringe. For each aliquot, the BiOBr nanoplates were removed by centrifuging the aliquot at 7000 rpm for 4 minutes. Fluorescence spectra of the supernatant taken from each aliquot were then measured in a quartz cuvette using a Cary Eclipse spectrometer. For the detection of resorufin produced from the reduction of resazurin, the excitation wavelength was set to 550 nm, and the emission range was 560 nm to 800 nm. For the detection of fluorescein produced from the oxidation of APF, the excitation wavelength was set to 450 nm, and the emission range was 460 nm to 800 nm. The slit widths for both excitation and emission were 4 nm. The scan rate was 600 nm/min, and the step size was 1 nm.

Single-molecule fluorescence microscopy. To prepare samples for single-molecule fluorescence, glass microscope coverslips (No. 1.5) were washed and dried under a flow of nitrogen. Next, a 30 μL colloidal suspension of the BiOBr nanoplates in ethanol was spin-coated onto the coverslip. The coverslip was dried under N_2 flow and annealed in an oven at 400°C for 15 minutes to immobilize the particles. Single-molecule fluorescence microscopy was performed on a Nikon N-STORM super-resolution microscopy system with a Nikon CFI-6-APO TIRF 1.49 NA 100× oil-immersion objective lens. The angle of the laser illumination (405-nm and either 488-nm or 561-nm) was adjusted to provide total internal reflection fluorescence (TIRF) excitation. A C-NSTORM QUAD filter cube (405/488/561/647, CHROMA, TRF89902-NK) was used to collect photons emitted from the fluorogenic probes. An Andor iXon 897 electron-multiplying CCD (160×160 nm^2 pixel size in object space) with single-photon sensitivity was used to detect the fluorescence bursts. The exposure time of the camera was 50 milliseconds.

To image the activation of APF during photocatalytic oxidation, a solution of 30 nM APF in phosphate buffer (pH 7.4) with 1 μM of KIO_3 (as a sacrificial oxidant) was added to the coverslip using a micropipette. A 405-nm laser was used to photoexcite the BiOBr nanoplates, and a 488-nm laser was used to excite fluorescein molecules produced by the oxidation of APF. To image the activation of resazurin during photocatalytic reduction, a solution of 40 nM resazurin with 1 μM of NH_2OH (as a sacrificial reductant) in phosphate buffer (pH 7.4) was used. A 405-nm laser was used to photoexcite the BiOBr nanoplates, and a 561-nm laser was used to excite resorufin molecules produced by the reduction of resazurin. Both solutions were purged with argon for 30 minutes before fluorescence imaging, and a plastic cover with a nitrogen inlet was used to limit exposure of the solution to air during image acquisition. When imaging both reactions sequentially on the same individual BiOBr nanoplate, we imaged APF oxidation before imaging the reduction of resazurin to limit photodoping of the particles.[53] All imaging times in this work were kept short (i.e., 2500 frames, 2.08 minutes) for the same reason. In between changing the imaging solutions, the coverslip was repeatedly washed with a solution of phosphate buffer (pH 7.4) until no fluorescence contamination was observed (see **Figure S11**).

To increase the concentration of defects in the nanoplates (e.g., oxygen vacancies and Bi^0), they were photodoped *in situ* as described in our previous report.[53] The activity of the nanoplates was first imaged using either APF or resazurin as described above. After imaging, the coverslip was repeatedly washed using deionized water. 50 μL of a phosphate buffer solution (pH 7.4) containing 1 μM of NH_2OH was then dropped onto the coverslip as a sacrificial reductant. The sample was then irradiated with the 405-nm laser of the microscope for 5 minutes. The NH_2OH solution was removed, the coverslip was washed again, and the activity of the nanoplate was

imaged a second time using the same probe (e.g., APF or resazurin). **Figure S22** compares the distributions of photon counts from single-molecule imaging before and after photodoping.

Image analysis and colocalization. All post-processing of the captured images was performed using the ThunderSTORM plugin[67] within ImageJ (http://rsb.info.nih.gov/ij/) and custom analysis scripts written in MATLAB (MathWorks, R2018b). Captured image stacks after offset subtraction using dark images were further background-corrected by a temporal median filter with a 200-frame sliding window.[52, 68] Single-molecule bursts in the corrected images were localized by using ThunderSTORM with default settings and custom camera parameters (see Section 8, **Supporting Information**). Detected photons per localization were obtained by summing up all photons within a region (5 × 5 pixels) centered at the localized positions. The estimated localization precision was calculated based on the photons detected and the estimated background, as previously described.[69] Localized single-molecule positions in each frame were grouped across consecutive frames to count intensity "bursts" of probe molecules on the BiOBr nanoplates (Section 10, **Supporting Information**). Two-dimensional activity maps of each nanoplate were then visualized by binning all single molecule bursts within 120 × 120 nm^2 bins. Colocalization of redox reactions was performed using a coordinate-based colocalization (CBC) analysis.[52, 59] The procedure for correcting for system drift caused by the washing procedure in-between imaging APF oxidation and resazurin reduction is described in Section 11 of the **Supporting Information**. CBC analysis calculates the colocalization between two super-resolution datasets directly using the localized coordinates of each molecule instead of the pixelized super-resolution reconstructions. Specifically, the spatial density surrounding each burst in the APF oxidation dataset was calculated from the neighboring bursts in both the APF and resazurin datasets within discs of radius r (from 50 to 500

nm in 50 nm steps). The ordered-rank correlation coefficient is calculated using the two sets of the density distributions. Each coefficient was scaled by a weighting factor, depending on the distance to the nearest neighbor, to eliminate false-positive colocalizations for bursts whose nearest neighbor is far away. The final value was assigned as the colocalization (CBC) score of each burst in the APF dataset, and scores for each burst in the resazurin reduction dataset were calculated similarly. Colocalization scores vary from −1, representing perfectly excluded (anticorrelated) localizations, to +1 for perfectly colocalized localizations (Section 11, **Supporting Information**).

Associated content.

Acknowledgements.

This material is based upon work supported by the National Science Foundation (NSF) under grant no. CHE-1753344 to B.S. and under grant no. ECCS-1653777 to M.D.L. Acknowledgment is made to the donors of the American Chemical Society Petroleum Research Fund for partial support of this research (award # PRF58165-DNI10). Electron microscopy and x-ray photoelectron spectroscopy were performed at the Institute of Materials Science & Engineering at Washington University. X-ray diffraction was performed in the Department of Earth and Planetary Sciences at Washington University.

Supporting Information Available: Additional experimental details on the materials used in these experiments, characterization of the structure and morphology of the nanoplates, sample preparation and instrumentation for single-molecule fluorescence microscopy, analysis and processing of super-resolution images, and colocalization analysis. Additional discussion of defect-induced absorption in the nanoplates. Supporting figures providing characterization of

BiOBr nanoplates by XRD, absorption spectroscopy, TEM, XPS, and DIC microscopy; ensemble fluorescence spectra for different photocatalytic transformations; quantitative characterization of APF and resazurin fluorescence bursts on BiOBr nanoplates during single-molecule imaging; activity maps for APF oxidation at longer times; comparison of the activity and on-times for the edges and middle of the nanoplates; activity map after washing a nanoplate when switching between probe solutions; colocalization analysis before and after drift correction; colocalization analysis using shorter imaging times; additional super-resolution activity maps and colocalization analysis of type I and type II BiOBr nanoplates; the average on-times of fluorescence bursts for regions with different CBC scores; the number of photons detected from fluorescence bursts before and after photodoping the nanoplates. Supporting table comparing the distributions of photon counts detected for fluorescence bursts.

References

1. Yu, J.; Kudo, A., Effects of Structural Variation on the Photocatalytic Performance of Hydrothermally Synthesized $BiVO_4$. *Advanced Functional Materials* **2006,** *16*, 2163-2169.
2. Xi, G.; Ye, J., Synthesis of Bismuth Vanadate Nanoplates with Exposed {001} Facets and Enhanced Visible-Light Photocatalytic Properties. *Chemical Communications* **2010**, 1893-1895.
3. Martin, D. J.; Umezawa, N.; Chen, X.; Ye, J.; Tang, J., Facet Engineered Ag_3PO_4 for Efficient Water Photooxidation. *Energy & Environmental Science* **2013,** *6*, 3380-3386.
4. Yu, J.; Low, J.; Xiao, W.; Zhou, P.; Jaroniec, M., Enhanced Photocatalytic CO_2-Reduction Activity of Anatase TiO_2 by Coexposed {001} and {101} Facets. *Journal of the American Chemical Society* **2014,** *136*, 8839-8842.
5. Zhu, W.; Shen, M.; Fan, G.; Yang, A.; Meyer, J. R.; Ou, Y.; Yin, B.; Fortner, J.; Foston, M.; Li, Z.; Zou, Z.; Sadtler, B., Facet-Dependent Enhancement in the Activity of Bismuth Vanadate Microcrystals for the Photocatalytic Conversion of Methane to Methanol. *ACS Applied Nano Materials* **2018,** *1*, 6683-6691.
6. Zhao, K.; Zhang, L.; Wang, J.; Li, Q.; He, W.; Yin, J. J., Surface Structure-Dependent Molecular Oxygen Activation of BiOCl Single-Crystalline Nanosheets. *Journal of the American Chemical Society* **2013,** *135*, 15750-15753.
7. Ye, L.; Zan, L.; Tian, L.; Peng, T.; Zhang, J., The {001} Facets-Dependent High Photoactivity of BiOCl Nanosheets. *Chemical Communications* **2011,** *47*, 6951-6953.
8. Shi, M.; Li, G.; Li, J.; Jin, X.; Tao, X.; Zeng, B.; Pidko, E. A.; Li, R.; Li, C., Intrinsic Facet-Dependent Reactivity of Well-Defined BiOBr Nanosheets on Photocatalytic Water Splitting. *Angewandte Chemie International Edition* **2020,** *59*, 6590-6595.

9. Chen, X.; Liu, L.; Yu, P. Y.; Mao, S. S., Increasing Solar Absorption for Photocatalysis with Black Hydrogenated Titanium Dioxide Nanocrystals. *Science* **2011,** *331*, 746-750.
10. Zhang, N.; Li, X.; Ye, H.; Chen, S.; Ju, H.; Liu, D.; Lin, Y.; Ye, W.; Wang, C.; Xu, Q.; Zhu, J.; Song, L.; Jiang, J.; Xiong, Y., Oxide Defect Engineering Enables to Couple Solar Energy into Oxygen Activation. *Journal of the American Chemical Society* **2016,** *138*, 8928-8935.
11. Guan, M.; Xiao, C.; Zhang, J.; Fan, S.; An, R.; Cheng, Q.; Xie, J.; Zhou, M.; Ye, B.; Xie, Y., Vacancy Associates Promoting Solar-Driven Photocatalytic Activity of Ultrathin Bismuth Oxychloride Nanosheets. *Journal of the American Chemical Society* **2013,** *135*, 10411-10417.
12. Li, H.; Shi, J.; Zhao, K.; Zhang, L., Sustainable Molecular Oxygen Activation with Oxygen Vacancies on the {001} Facets of BiOCl Nanosheets under Solar Light. *Nanoscale* **2014,** *6*, 14168-14173.
13. Wang, X.-j.; Zhao, Y.; Li, F.-t.; Dou, L.-j.; Li, Y.-p.; Zhao, J.; Hao, Y.-j., A Chelation Strategy for In-Situ Constructing Surface Oxygen Vacancy on {001} Facets Exposed BiOBr Nanosheets. *Scientific Reports* **2016,** *6*, 24918.
14. Wang, H.; Yong, D.; Chen, S.; Jiang, S.; Zhang, X.; Shao, W.; Zhang, Q.; Yan, W.; Pan, B.; Xie, Y., Oxygen-Vacancy-Mediated Exciton Dissociation in BiOBr for Boosting Charge-Carrier-Involved Molecular Oxygen Activation. *Journal of the American Chemical Society* **2018,** *140*, 1760-1766.
15. Mao, C.; Cheng, H.; Tian, H.; Li, H.; Xiao, W.-J.; Xu, H.; Zhao, J.; Zhang, L., Visible Light Driven Selective Oxidation of Amines to Imines with BiOCl: Does Oxygen Vacancy Concentration Matter? *Applied Catalysis B: Environmental* **2018,** *228*, 87-96.
16. Li, H.; Shang, J.; Zhu, H.; Yang, Z.; Ai, Z.; Zhang, L., Oxygen Vacancy Structure Associated Photocatalytic Water Oxidation of BiOCl. *ACS Catalysis* **2016,** *6*, 8276-8285.

17. Di, J.; Chen, C.; Yang, S.-Z.; Ji, M.; Yan, C.; Gu, K.; Xia, J.; Li, H.; Li, S.; Liu, Z., Defect Engineering in Atomically-Thin Bismuth Oxychloride Towards Photocatalytic Oxygen Evolution. *Journal of Materials Chemistry A* **2017,** *5*, 14144-14151.

18. Wu, J.; Li, X.; Shi, W.; Ling, P.; Sun, Y.; Jiao, X.; Gao, S.; Liang, L.; Xu, J.; Yan, W.; Wang, C.; Xie, Y., Efficient Visible-Light-Driven CO_2 Reduction Mediated by Defect-Engineered BiOBr Atomic Layers. *Angewandte Chemie International Edition* **2018,** *57*, 8719-8723.

19. Li, H.; Shang, J.; Ai, Z.; Zhang, L., Efficient Visible Light Nitrogen Fixation with BiOBr Nanosheets of Oxygen Vacancies on the Exposed {001} Facets. *Journal of the American Chemical Society* **2015,** *137*, 6393-6399.

20. Xue, X.; Chen, R.; Chen, H.; Hu, Y.; Ding, Q.; Liu, Z.; Ma, L.; Zhu, G.; Zhang, W.; Yu, Q.; Liu, J.; Ma, J.; Jin, Z., Oxygen Vacancy Engineering Promoted Photocatalytic Ammonia Synthesis on Ultrathin Two-Dimensional Bismuth Oxybromide Nanosheets. *Nano Letters* **2018,** *18*, 7372-7377.

21. Kato, H.; Asakura, K.; Kudo, A., Highly Efficient Water Splitting into H_2 and O_2 over Lanthanum-Doped $NaTaO_3$ Photocatalysts with High Crystallinity and Surface Nanostructure. *Journal of the American Chemical Society* **2003,** *125*, 3082-3089.

22. Ohno, T.; Sarukawa, K.; Matsumura, M., Crystal Faces of Rutile and Anatase TiO_2 Particles and Their Roles in Photocatalytic Reactions. *New Journal of Chemistry* **2002,** *26*, 1167-1170.

23. Giocondi, J. L.; Salvador, P. A.; Rohrer, G. S., The Origin of Photochemical Anisotropy in $SrTiO_3$. *Topics in Catalysis* **2007,** *44*, 529-533.

24. Matsumoto, Y.; Ida, S.; Inoue, T., Photodeposition of Metal and Metal Oxide at the TiO_x Nanosheet to Observe the Photocatalytic Active Site. *The Journal of Physical Chemistry C* **2008,** *112*, 11614-11616.

25. Murakami, N.; Kurihara, Y.; Tsubota, T.; Ohno, T., Shape-Controlled Anatase Titanium(IV) Oxide Particles Prepared by Hydrothermal Treatment of Peroxo Titanic Acid in the Presence of Polyvinyl Alcohol. *The Journal of Physical Chemistry C* **2009,** *113*, 3062-3069.

26. Sabio, E. M.; Chi, M.; Browning, N. D.; Osterloh, F. E., Charge Separation in a Niobate Nanosheet Photocatalyst Studied with Photochemical Labeling. *Langmuir* **2010,** *26*, 7254-7261.

27. Li, R.; Zhang, F.; Wang, D.; Yang, J.; Li, M.; Zhu, J.; Zhou, X.; Han, H.; Li, C., Spatial Separation of Photogenerated Electrons and Holes among {010} and {110} Crystal Facets of $BiVO_4$. *Nature Communications* **2013,** *4*, 1432.

28. Zhang, L.; Wang, W.; Sun, S.; Jiang, D.; Gao, E., Selective Transport of Electron and Hole among {001} and {110} Facets of BiOCl for Pure Water Splitting. *Applied Catalysis B: Environmental* **2015,** *162*, 470-474.

29. Wang, B.; Shen, S.; Guo, L., $SrTiO_3$ Single Crystals Enclosed with High-Indexed {023} Facets and {001} Facets for Photocatalytic Hydrogen and Oxygen Evolution. *Applied Catalysis B: Environmental* **2015,** *166-167*, 320-326.

30. Mu, L.; Zhao, Y.; Li, A.; Wang, S.; Wang, Z.; Yang, J.; Wang, Y.; Liu, T.; Chen, R.; Zhu, J.; Fan, F.; Li, R.; Li, C., Enhancing Charge Separation on High Symmetry $SrTiO_3$ Exposed with Anisotropic Facets for Photocatalytic Water Splitting. *Energy & Environmental Science* **2016,** *9*, 2463-2469.

31. Wenderich, K.; Mul, G., Methods, Mechanism, and Applications of Photodeposition in Photocatalysis: A Review. *Chemical Reviews* **2016,** *116*, 14587-14619.

32. Guo, Y.; Siretanu, I.; Zhang, Y.; Mei, B.; Li, X.; Mugele, F.; Huang, H.; Mul, G., pH-Dependence in Facet-Selective Photo-Deposition of Metals and Metal Oxides on Semiconductor Particles. *Journal of Materials Chemistry A* **2018,** *6*, 7500-7508.

33. Cortés, E.; Xie, W.; Cambiasso, J.; Jermyn, A. S.; Sundararaman, R.; Narang, P.; Schlücker, S.; Maier, S. A., Plasmonic Hot Electron Transport Drives Nano-Localized Chemistry. *Nature Communications* **2017,** *8*, 14880.

34. Roeffaers, M. B. J.; Sels, B. F.; Uji-i, H.; Schryver, F. C. D.; Jacobs, P. A.; Vos, D. E. D.; Hofkens, J., Spatially Resolved Observation of Crystal-Face-Dependent Catalysis by Single Turnover Counting. *Nature* **2006,** *439*, 572-575.

35. Ristanović, Z.; Hofmann, J. P.; De Cremer, G.; Kubarev, A. V.; Rohnke, M.; Meirer, F.; Hofkens, J.; Roeffaers, M. B. J.; Weckhuysen, B. M., Quantitative 3D Fluorescence Imaging of Single Catalytic Turnovers Reveals Spatiotemporal Gradients in Reactivity of Zeolite H-ZSM-5 Crystals Upon Steaming. *Journal of the American Chemical Society* **2015,** *137*, 6559-6568.

36. Roeffaers, M. B. J.; De Cremer, G.; Libeert, J.; Ameloot, R.; Dedecker, P.; Bons, A.-J.; Bückins, M.; Martens, J. A.; Sels, B. F.; De Vos, D. E.; Hofkens, J., Super-Resolution Reactivity Mapping of Nanostructured Catalyst Particles. *Angewandte Chemie International Edition* **2009,** *48*, 9285-9289.

37. Wang, N.; Tachikawa, T.; Majima, T., Single-Molecule, Single-Particle Observation of Size-Dependent Photocatalytic Activity in Au/TiO_2 Nanocomposites. *Chemical Science* **2011,** *2*, 891-900.

38. Tachikawa, T.; Yamashita, S.; Majima, T., Evidence for Crystal-Face-Dependent TiO_2 Photocatalysis from Single-Molecule Imaging and Kinetic Analysis. *Journal of the American Chemical Society* **2011,** *133*, 7197-7204.

39. Tachikawa, T.; Yonezawa, T.; Majima, T., Super-Resolution Mapping of Reactive Sites on Titania-Based Nanoparticles with Water-Soluble Fluorogenic Probes. *ACS Nano* **2013,** *7*, 263-275.

40. Xu, W.; Jain, P. K.; Beberwyck, B. J.; Alivisatos, A. P., Probing Redox Photocatalysis of Trapped Electrons and Holes on Single Sb-Doped Titania Nanorod Surfaces. *Journal of the American Chemical Society* **2012,** *134*, 3946-3949.

41. Zhang, Y.; Lucas, J. M.; Song, P.; Beberwyck, B.; Fu, Q.; Xu, W.; Alivisatos, A. P., Superresolution Fluorescence Mapping of Single-Nanoparticle Catalysts Reveals Spatiotemporal Variations in Surface Reactivity. *Proceedings of the National Academy of Sciences* **2015,** *112*, 8959-8964.

42. Sambur, J. B.; Chen, T.-Y.; Choudhary, E.; Chen, G.; Nissen, E. J.; Thomas, E. M.; Zou, N.; Chen, P., Sub-Particle Reaction and Photocurrent Mapping to Optimize Catalyst-Modified Photoanodes. *Nature* **2016,** *530*, 77-80.

43. Mao, X.; Liu, C.; Hesari, M.; Zou, N.; Chen, P., Super-Resolution Imaging of Non-Fluorescent Reactions Via Competition. *Nature Chemistry* **2019,** *11*, 687-694.

44. Ha, J. W.; Ruberu, T. P. A.; Han, R.; Dong, B.; Vela, J.; Fang, N., Super-Resolution Mapping of Photogenerated Electron and Hole Separation in Single Metal–Semiconductor Nanocatalysts. *Journal of the American Chemical Society* **2014,** *136*, 1398-1408.

45. Xu, W.; Kong, J. S.; Yeh, Y.-T. E.; Chen, P., Single-Molecule Nanocatalysis Reveals Heterogeneous Reaction Pathways and Catalytic Dynamics. *Nature Materials* **2008,** *7*, 992-996.

46. Zhou, X.; Xu, W.; Liu, G.; Panda, D.; Chen, P., Size-Dependent Catalytic Activity and Dynamics of Gold Nanoparticles at the Single-Molecule Level. *Journal of the American Chemical Society* **2010,** *132*, 138-146.

47. Zhou, X.; Andoy, N. M.; Liu, G.; Choudhary, E.; Han, K.-S.; Shen, H.; Chen, P., Quantitative Super-Resolution Imaging Uncovers Reactivity Patterns on Single Nanocatalysts. *Nature Nanotechnology* **2012,** *7*, 237-241.

48. Zou, N.; Chen, G.; Mao, X.; Shen, H.; Choudhary, E.; Zhou, X.; Chen, P., Imaging Catalytic Hotspots on Single Plasmonic Nanostructures Via Correlated Super-Resolution and Electron Microscopy. *ACS Nano* **2018,** *12*, 5570-5579.

49. Chen, T.; Zhang, Y.; Xu, W., Single-Molecule Nanocatalysis Reveals Catalytic Activation Energy of Single Nanocatalysts. *Journal of the American Chemical Society* **2016,** *138*, 12414-12421.

50. Chen, T.; Dong, B.; Chen, K.; Zhao, F.; Cheng, X.; Ma, C.; Lee, S.; Zhang, P.; Kang, S. H.; Ha, J. W.; Xu, W.; Fang, N., Optical Super-Resolution Imaging of Surface Reactions. *Chemical Reviews* **2017,** *117*, 7510-7537.

51. Wang, W.-K.; Chen, J.-J.; Lou, Z.-Z.; Kim, S.; Fujitsuka, M.; Yu, H.-Q.; Majima, T., Single-Molecule and -Particle Probing Crystal Edge/Corner as Highly Efficient Photocatalytic Sites on a Single TiO_2 Particle. *Proceedings of the National Academy of Sciences* **2019,** *116*, 18827-18833.

52. Shen, M.; Ding, T.; Hartman, S. T.; Wang, F.; Krucylak, C.; Wang, Z.; Tan, C.; Yin, B.; Mishra, R.; Lew, M. D.; Sadtler, B., Nanoscale Colocalization of Fluorogenic Probes Reveals the Role of Oxygen Vacancies in the Photocatalytic Activity of Tungsten Oxide Nanowires. *ACS Catalysis* **2020,** *10*, 2088-2099.

53. Shen, M.; Ding, T.; Luo, J.; Tan, C.; Mahmood, K.; Wang, Z.; Zhang, D.; Mishra, R.; Lew, M. D.; Sadtler, B., Competing Activation and Deactivation Mechanisms in Photodoped Bismuth Oxybromide Nanoplates Probed by Single-Molecule Fluorescence Imaging. *The Journal of Physical Chemistry Letters* **2020,** *11*, 5219-5227.

54. Easter, Q. T.; Garcia, A.; Blum, S. A., Single-Polymer–Particle Growth Kinetics with Molecular Catalyst Speciation and Single-Turnover Imaging. *ACS Catalysis* **2019,** *9*, 3375-3383.

55. Garcia IV, A.; Saluga, S. J.; Dibble, D. J.; López, P. A.; Saito, N.; Blum, S. A., Does Selectivity of Molecular Catalysts Change with Time? Polymerization Imaged by Single-Molecule Spectroscopy. *Angewandte Chemie International Edition* **2021,** *60*, 1550-1555.

56. Wu, S.; Sun, W.; Sun, J.; Hood, Z. D.; Yang, S.-Z.; Sun, L.; Kent, P. R. C.; Chisholm, M. F., Surface Reorganization Leads to Enhanced Photocatalytic Activity in Defective BiOCl. *Chemistry of Materials* **2018,** *30*, 5128-5136.

57. Feng, H.; Xu, Z.; Wang, L.; Yu, Y.; Mitchell, D.; Cui, D.; Xu, X.; Shi, J.; Sannomiya, T.; Du, Y.; Hao, W.; Dou, S. X., Modulation of Photocatalytic Properties by Strain in 2D BiOBr Nanosheets. *ACS Applied Materials & Interfaces* **2015,** *7*, 27592-27596.

58. Wu, D.; Yue, S.; Wang, W.; An, T.; Li, G.; Ye, L.; Yip, H. Y.; Wong, P. K., Influence of Photoinduced Bi-Related Self-Doping on the Photocatalytic Activity of BiOBr Nanosheets. *Applied Surface Science* **2017,** *391*, 516-524.

59. Malkusch, S.; Endesfelder, U.; Mondry, J.; Gelléri, M.; Verveer, P. J.; Heilemann, M., Coordinate-Based Colocalization Analysis of Single-Molecule Localization Microscopy Data. *Histochemistry and Cell Biology* **2012,** *137*, 1-10.

60. Liu, J.; Hill, C. M.; Pan, S.; Liu, H., Interfacial Charge Transfer Events of BODIPY Molecules: Single Molecule Spectroelectrochemistry and Substrate Effects. *Physical Chemistry Chemical Physics* **2014,** *16*, 23150-23156.

61. Evans, R. C.; Ellingworth, A.; Cashen, C. J.; Weinberger, C. R.; Sambur, J. B., Influence of Single-Nanoparticle Electrochromic Dynamics on the Durability and Speed of Smart Windows. *Proceedings of the National Academy of Sciences* **2019,** *116*, 12666-12671.

62. Kamat, P. V.; Jin, S., Semiconductor Photocatalysis: "Tell Us the Complete Story!". *ACS Energy Letters* **2018,** *3*, 622-623.

63. Naldoni, A.; Altomare, M.; Zoppellaro, G.; Liu, N.; Kment, Š.; Zbořil, R.; Schmuki, P., Photocatalysis with Reduced TiO_2: From Black TiO_2 to Cocatalyst-Free Hydrogen Production. *ACS Catalysis* **2019,** *9*, 345-364.

64. Pinaud, B. A.; Benck, J. D.; Seitz, L. C.; Forman, A. J.; Chen, Z.; Deutsch, T. G.; James, B. D.; Baum, K. N.; Baum, G. N.; Ardo, S.; Wang, H.; Miller, E.; Jaramillo, T. F., Technical and Economic Feasibility of Centralized Facilities for Solar Hydrogen Production Via Photocatalysis and Photoelectrochemistry. *Energy & Environmental Science* **2013,** *6*, 1983-2002.

65. Wu, K.; Lian, T., Quantum Confined Colloidal Nanorod Heterostructures for Solar-to-Fuel Conversion. *Chemical Society Reviews* **2016,** *45*, 3781-3810.

66. Zhang, S.; Si, Y.; Li, B.; Yang, L.; Dai, W.; Luo, S., Atomic-Level and Modulated Interfaces of Photocatalyst Heterostructure Constructed by External Defect-Induced Strategy: A Critical Review. *Small* **2021,** *17*, 2004980.

67. Ovesný, M.; Křížek, P.; Borkovec, J.; Švindrych, Z.; Hagen, G. M., ThunderSTORM: A Comprehensive ImageJ Plug-in for PALM and STORM Data Analysis and Super-Resolution Imaging. *Bioinformatics* **2014,** *30*, 2389-2390.

68. Hoogendoorn, E.; Crosby, K. C.; Leyton-Puig, D.; Breedijk, R. M. P.; Jalink, K.; Gadella, T. W. J.; Postma, M., The Fidelity of Stochastic Single-Molecule Super-Resolution Reconstructions Critically Depends Upon Robust Background Estimation. *Scientific Reports* **2014,** *4*, 3854.

69. Rieger, B.; Stallinga, S., The Lateral and Axial Localization Uncertainty in Super-Resolution Light Microscopy. *ChemPhysChem* **2014,** *15*, 664-670.

TOC graphic

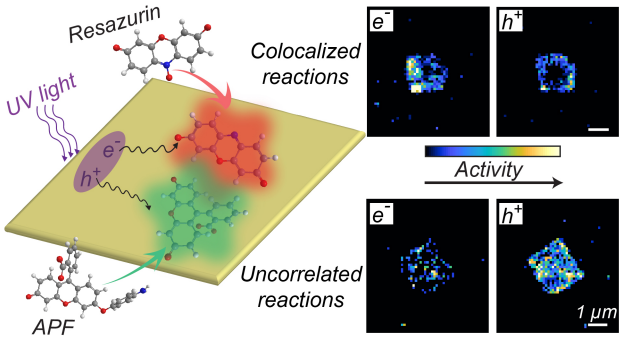
Resazurin
UV light
e⁻
h⁺
APF⁻
Colocalized reactions
Uncorrelated reactions
e⁻
h⁺
Activity
e⁻
h⁺
1 μm